 doi:10.20944/preprints202207.0061.v1

Article

Coastal Upwelling in the Bay of Bengal: Role of Local and Remote Windstress

Sthitapragya Ray [1], Debadatta Swain [1]*, M.M. Ali [2,3], Mark A. Bourassa [2,4]

[1] 1School of Earth, Ocean and Climate Sciences, Indian Institute of Technology Bhubaneswar, Argul, Jatni – 752050, India; sr35@iitbbs.ac.in (S.R.)
[2] 2Center for Ocean-Atmospheric Prediction Studies, The Florida State University, Tallahassee, FL 32306, USA; mmali@coaps.fsu.edu (M.M.A.); bourassa@coaps.fsu.edu (M.A.B.)
[3] Andhra Pradesh State Disaster Management Authority, Kunchanapalle 522501, India
[4] Department of Earth, Ocean and Atmospheric Science, The Florida State University, Tallahassee, FL 32306, USA
* Correspondence: dswain@iitbbs.ac.in

Abstract: Monsoon winds drive upwelling along the eastern coast of India during the south-west (SW) monsoons. These winds also provide alongshore windstress (AWS) resulting in positive cross-shore Ekman transport (ET) from late May to the end of September. While instances of high ET and sea surface temperature (SST) based upwelling index (UISST) were observed along different parts of the coast, UISST was weaker in the northern section in the earlier part of monsoon. This was even in the presence of maximum AWS and ET during the 10 years analysis period spanning January-2009 to December-2018. Additionally, negative sea surface height anomalies (SSHAs), typically associated with coastal upwelling, were observed only along the southern-most coast. An empirical orthogonal function (EOF) analysis revealed two coherent modes of SSHA variation. The first principal component (PC) showed a SSHA signature coincident spatio-temporally with the first downwelling Kelvin wave, closely associated with the equatorial zonal winds that drive coastal Kelvin waves. The third PC with a coastal SSHA pattern similar to the second upwelling Kelvin wave was associated with offshore ET along the northern part of the Indian east coast. Time series of the two PCs exhibited suppression of coastal upwelling by downwelling Kelvin waves during May-July along the northeastern coast of India. Local AWS driven ET was the primary driver of coastal upwelling with the weakening of the remotely forced Kelvin waves in August. A coherent mode consisting of negative coastal SSHA signature was excited in response to local AWS driven ET during the upwelling period. This study examined the spatio-temporal variability of SW monsoon coastal upwelling along the east coast of India and illustrated the role of equatorial windstress forced first downwelling Kelvin wave in suppressing upwelling in the northern part of the coast during early SW monsoon season.

Keywords: Coastal upwelling; Upwelling index; Scatterometer; Wind stress; Kelvin Wave; Ekman Transport

1. Introduction

Coastal upwelling is associated with the upward flow of nutrient–rich subsurface waters into the euphotic layer as a result of the wind-induced divergence of surface currents along the coast. These upwelled waters, in turn, result in phytoplankton blooms, which support large zooplankton populations along with larger marine organisms [1]. This makes the major upwelling regions some of the most productive parts of the global oceans. In fact, the major coastal upwelling systems associated with eastern boundary currents, which comprise 1% of total ocean surface area contribute 20% of global fish production [2]. In addition, understanding coastal upwelling is also necessary as it plays an important role in mediating various air-sea fluxes, including the air-sea CO_2 flux [3]. The major perennial coastal upwelling systems of the world, namely, California, Peru-Chile,

 doi:10.20944/preprints202207.0061.v1

Portugal-Northwest Africa, and Southwest Africa are called the Eastern Boundary Upwelling Systems (EBUS) [4]. Further, several seasonal coastal upwelling systems also exist along the eastern and western boundaries of various ocean basins.

A positive along-shore windstress (AWS) (northward winds for east-facing coasts in the northern hemisphere) is known to set up the cross-shore surface currents directed off-shore (positive Ekman Transport (ET)) thereby producing a coastal divergence of currents [4]. Subsequent geostrophic adjustment then creates an alongshore surface flow in the direction of the wind. Thus, the ET could serve as a proxy upwelling index (based on wind-stress). Since coastal upwelling brings relatively cooler waters closer to the coast, the near-shore gradient of Sea Surface Temperature (SST) is also often used as a proxy upwelling index (SST-based UI: UI_{SST}). In addition to this, negative coastal SSHAs are indicators of coastal upwelling as well.

The seasonal upwelling systems in the North Indian Ocean (NIO), like those along the coasts of Somalia, Oman, western and eastern India and Sri Lanka are associated with the seasonally reversing southwest (SW) monsoon winds [4]. The seasonal upwelling system along the western margin of the Bay of Bengal (BoB) is driven by southwesterly monsoon winds which align parallel to the coast from April with peak values during June—September and set up a narrow (30-40 km wide) upwelling zone along most of the coastline (11-18 °N). Runoff from some of the major rivers like the Ganga, Brahmaputra, and Mahanadi in the Indian sub-continent, which also peak during June-September periods, suppresses upwelling signatures towards the northern parts of the coast [5]. The hydrographic analysis of [6] also observed sea surface signatures consistent with coastal upwelling at 18 °N, 87 °E (north-eastern BoB) during September 1996. Similar observations of coastal upwelling were made by [7] along the stretch of the east coast of India from 16° 30′ N to 18° 30′ N in hydrographic data. Coastal upwelling signatures have also been identified along the stretch of the coast between Chennai (13.082 °N) and Vishakapatnam (17.687 °N) based on satellite SST data [8]. [9] has analysed the long-term variability of coastal upwelling along the eastern coast of south India using UI_{SST} and AWS; this closely resembles the methods adopted in the present analysis.

In the present analysis, we have examined the spatio-temporal variability of the coastal upwelling system in the BoB during SW monsoon based on several remotely sensed reanalysis datasets and attempt to explore the role of local and remote surface wind forcing in driving this upwelling system. Our analysis agreed closely with previous *in situ* studies, which have observed a limited impact of remote forcing in this system. However, very interestingly, the coastally trapped first downwelling Kelvin wave appeared to suppress coastal upwelling in the north BoB, compared to the south along the Indian east coast.

2. Data Used

The analysis was carried out utilizing three sets of remote-sensing reanalyses data products spanning the period from 2009 to 2018 (Table 1). These data sets consisted of 6-hourly winds from Institut Français de Recherche pour l'Exploitation de la Mer (IFREMER), daily Operational SST and Ice Analysis (OSTIA) SST, and Integrated Multi-Mission Ocean Altimeter Data for Climate Research (MEaSUREs) SSHA at a temporal resolution of 5 days. 6-hourly gridded winds at a grid spacing of 0.25° are available from IFREMER through Copernicus Marine Environment Monitoring Service (CMEMS). 10-m L2B equivalent neutral winds swath-data from multiple scatterometer missions (ERS-1 to Scatsat-1) are combined with ancillary data from radiometers (SSM/I, SSMIS) and atmospheric wind reanalysis (ERA-interim or ERA-5) to generate this gridded gap-free wind data product. We have used zonal and meridional wind stress data obtained from these data products. The product user manual and quality information document for this dataset are available through CMEMS [10]. Intercomparison of these wind products with ERA 5 wind vectors yielded a wind speed root mean square difference (RMSD) of 1.87

Preprints (www.preprints.org) | NOT PEER-REVIEWED | Posted: 5 July 2022 doi:10.20944/preprints202207.0061.v1

m/s close to the coast, and the vector correlation between the two wind direction data was 1.63 near the coast (out of a maximum possible value of 2.0) [11].

The OSTIA L4 daily SST provides gridded SST data at a grid spacing of 0.05° generated from the combination of observations from multiple IR and microwave sensors [12]. The product user manual [13] and quality information document [12] for this dataset are available through CMEMS. The product has a mean difference of 0.06 °C for the global oceans, and 0.02 °C for the Indian Ocean in comparison with in-situ SST observations from ARGO floats [12].

SSHA data from JPL MEaSUREs Gridded SSHAs Version JPL1812, a part of the Integrated Multi-Mission Ocean Altimeter Data for Climate Research [14] developed by the NASA Making Earth System Data Records for Use in Research Environments (MEaSUREs) Program has been used in the present analysis [15]. This dataset with a temporal resolution of 5 days and a grid spacing of 0.25° involved observations from available altimeters like TOPEX/Poseidon, Jason-1, Jason-2, Jason-3 and one among ERS-1, ERS-2, EnviSat, Cryosat-2, AltiKa, and Sentinel-3A [15]. [15] also reported an RMSD of 2.5 – 7.5 cm (depending on location), and a global RMSD of up to 5.62 cm on validation of the generated products by intercomparison with tide gauges and altimeters, respectively. In addition, the Global Self-consistent Hierarchical High-resolution Geography (GSHHG) version 2.3.7 L1 shorelines dataset [16] was used in the present analysis.

Table 1. Details of Datasets used.

Parameter	Dataset	Grid Spacing	Temporal Resolution
Zonal & Meridional Windstress	CMEMS WIND_GLO_WIND_L4 _REP_OBSERVATIONS_012_006	0.25° × 0.25°	6 hour
Sea Surface Temperature	OSTIA Near Real Time Level 4 SST	0.05° × 0.05°	Daily
Sea Surface Height Anomaly	JPL MEASURES Gridded Sea Surface Height Anomalies	0.25° × 0.25°	5 day

3. Methodology

The analysis involved proper identification of the spatial and temporal extent of the coastal upwelling processes along the Indian coast as the preliminary step [5 – 8]. Consequently, the coastline between 10.25 °N and 19 °N, and 78 °E to 90 °E with upwelling features was identified for carrying out the intended analysis. In addition to these coastal points, the entire Bay of Bengal (5 – 25 °N, 78 – 100 °E) was selected as the study area for the principal component (PC) analysis. Windstress and SST data were sampled to a temporal resolution of 5 days centered on the date of the SSHA dataset. For this, a mean of the high temporal resolution data (SST and windstress) over the period of the low resolution data (SSHA) was considered whenever a direct comparison was necessary.

The coastline was first extracted from the GSHHG coastline dataset. Subsequently, the coastline was simplified by manually rejecting points where multiple points were present in close proximity to the complex coastal features of scales comparable to 0.25° distance. In the case of enclosed bays, the inner points were rejected while the outer ones were retained. This allowed us to obtain distinct coastal locations for the analysis, thus resulting in a set of 23 coastal points for the present study (Figure 1). AWS, UI_{SST} , and SSHA were sampled at each of these coastal points and their decadal climatology (2009 – 2018) were analysed focusing on the pre-monsoon (May) and SW monsoon (June – September) seasons. The computation of UI_{SST} required a second set of 23 offshore points (one for each coastal point) that were located at the same latitude but 3° east of the corresponding coastal point, as discussed later. In addition, the entire spatial SSHA dataset over the full 2009 – 2018 period (not restricted to pre-monsoon and monsoon seasons) was also

Preprints (www.preprints.org) | NOT PEER-REVIEWED | Posted: 5 July 2022 doi:10.20944/preprints202207.0061.v1

used to carry out an Empirical Orthogonal Function (EOF) analysis to investigate the role of coastally trapped Kelvin waves in modulating this upwelling system. These methods are further described in the following subsections. Figure 2 presents a schematic of the entire methodology used in the present analysis.

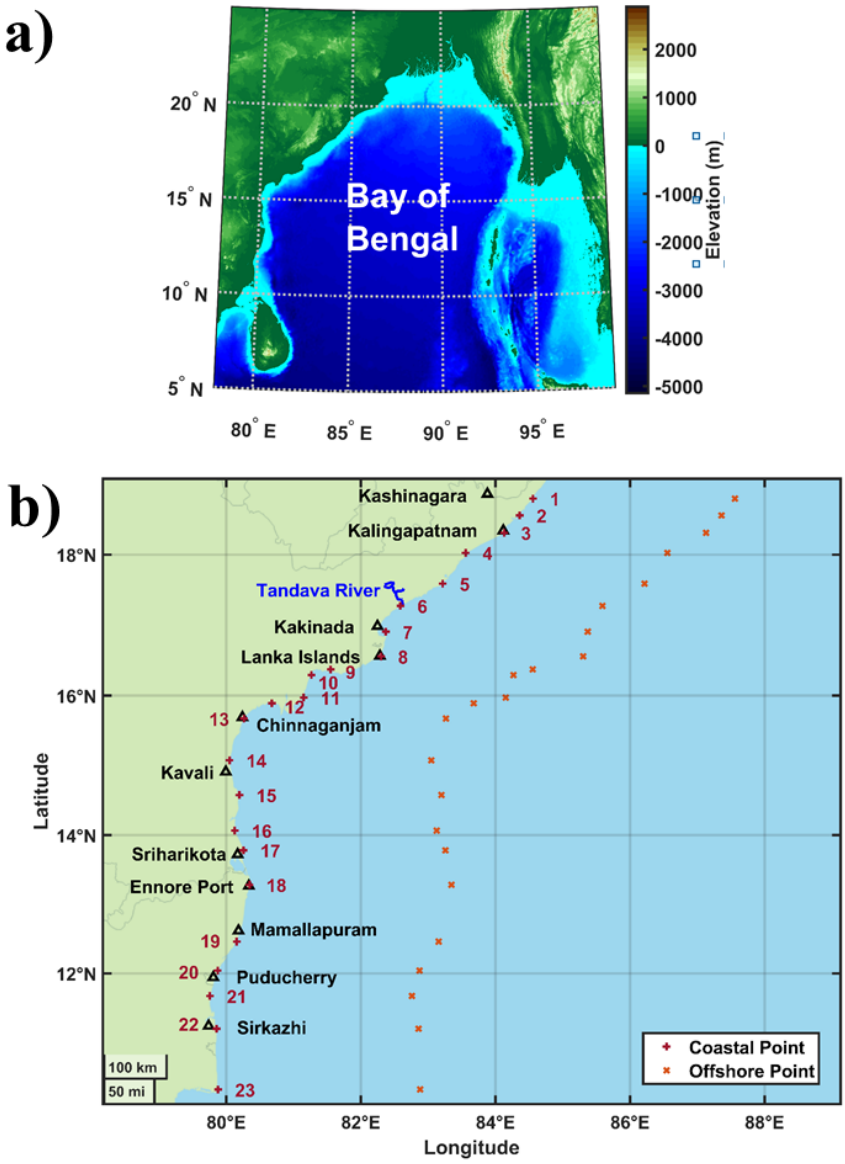

Figure 1. (a) Study area with overlaid bathymetry, (b) Coastal observation points and corresponding offshore points.

Preprints (www.preprints.org) | NOT PEER-REVIEWED | Posted: 5 July 2022 doi:10.20944/preprints202207.0061.v1

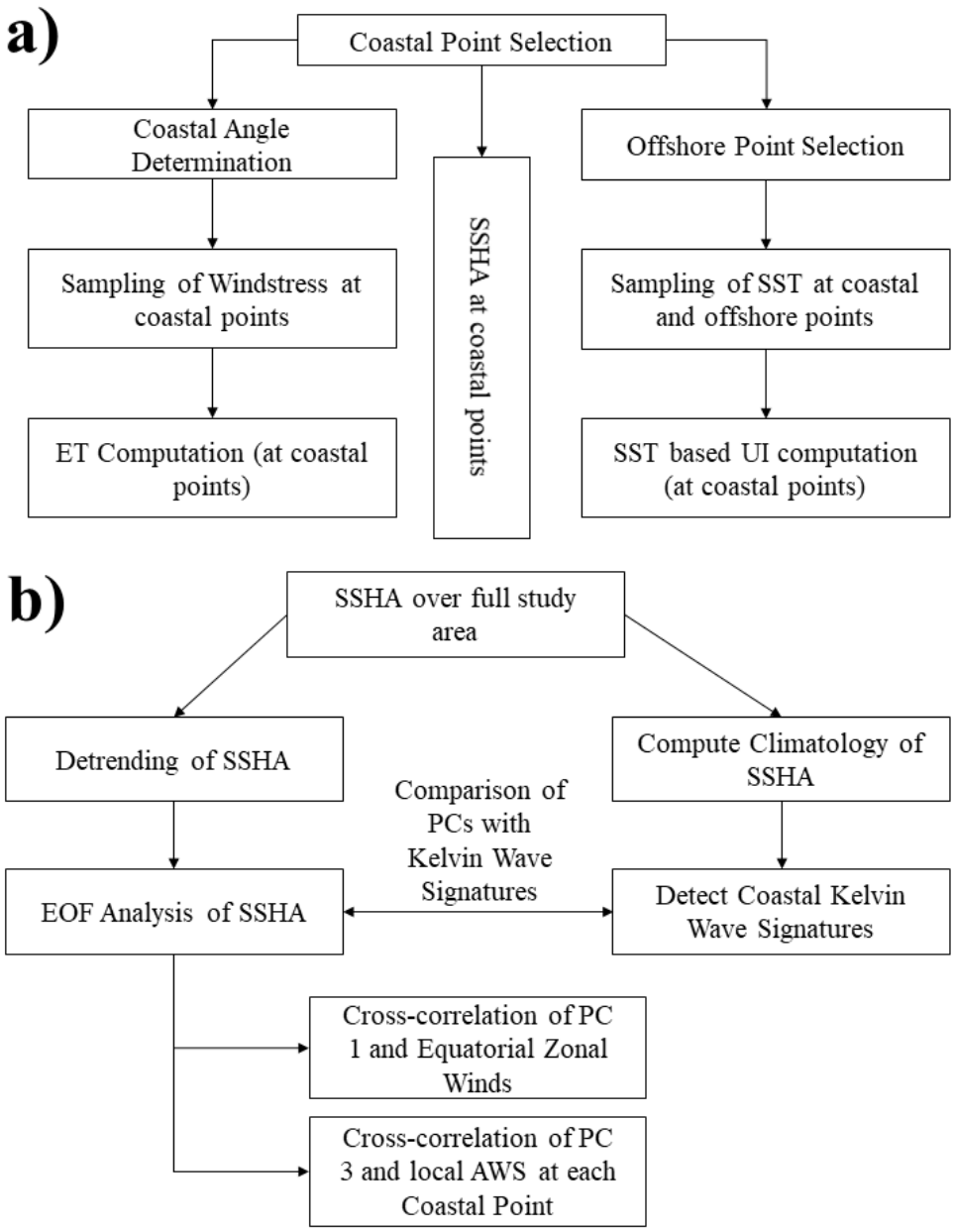

Figure 2. (a) Methodology of computation of upwelling indicators at the coastal points, (b) Analysis of spatial SSHA for detection of coastal Kelvin waves.

3.1. Estimation of Coastal Angles

The traditional method of estimation of coastal angles involved a visual estimation of the slope of the coastline as demonstrated by [17] for the west coast of North America over a 200 mile (322 km) section based on bathymetric charts. [18] used a similar method in the Canary current upwelling system utilizing the gridded relief model ETOPO1 based on the mean slope of the 200 m isobaths line over a segment of the length of roughly 80 km. [19] used a straight line inclined at 24° to approximate the western coast of India from 10° to 20 °N [18]. [20] extended the same approximation down to the southern tip of India in their analyses involving the use of coastal angles. Similar simplified approximations for the coastline were also used by [21] in their analysis of coastal upwelling along the KwaZulu Natal Bight in South Africa. To determine the orientation of the coastline in the present analysis, at each of the 23 coastal points, the coast was partitioned into two lines that converged at that given point. The two lines on either side of the given point were then

Preprints (www.preprints.org) | NOT PEER-REVIEWED | Posted: 5 July 2022 doi:10.20944/preprints202207.0061.v1

simplified using the Douglas-Peucker line simplification algorithm (with varying tolerance parameter values) [22] and point closest to the given location was connected to form a line segment parallel to the coast at that point. The orientation of the new line then determined the coastal angle. The coastal angle values for different tolerance parameters are tabulated as Table 2. It may be noted that the tolerance value of 2.5° (in terms of distance centred about a coastal point) resulted in the entire stretch of the coastline to be approximated as a single straight line, the simplest possible approximation. Three different approximations of the coastline around point 11 based on three different tolerance values are demonstrated in Figure 3. ET corresponding to the lowest tolerance parameter value of 0.25° (5th column of Table 2) was used for the entire analysis. However, for comparative purposes, we also presented results for two tolerance values for coastline simplification, 0.25° and 1° (5th and 7th columns of Table 2) centred around the coastal points.

Table 2. Values of Coastal Angles corresponding to different tolerances at each coastal point.

Point Identifier	Geographic Reference	Latitude	Longitude	Tolerance value for coastal angle determination (distances)			
				0.25°	0.5°	1.0°	2.5°
1	Kashinagara	18.790	84.558	307.881	305.986	305.986	328.321
2	-	18.554	84.359	307.881	305.986	305.986	328.321
3	Kalingapatnam	18.309	84.129	307.881	305.986	305.986	328.321
4	-	18.026	83.557	307.881	305.986	305.986	328.321
5	-	17.590	83.215	307.881	305.986	305.986	328.321
6	Tandava river mouth	17.276	82.589	314.701	305.986	305.986	328.321
7	Kakinada	16.909	82.371	310.404	305.986	305.986	328.321
8	Lanka Islands	16.558	82.303	303.787	305.986	305.986	328.321
9	-	16.372	81.553	301.885	305.986	328.321	328.321
10	-	16.293	81.267	301.885	309.486	328.321	328.321
11	-	15.972	81.152	293.506	309.486	328.321	328.321
12	-	15.889	80.677	305.507	309.486	328.321	328.321
13	Chinnaganjam	15.672	80.264	329.142	331.124	328.321	328.321
14	Kavali	15.074	80.048	361.978	331.124	328.321	328.321
15	-	14.577	80.196	355.912	355.912	328.321	328.321
16	-	14.066	80.126	361.978	355.912	328.321	328.321
17	Sriharikota	13.782	80.257	352.805	355.912	349.842	328.321
18	Ennore Port	13.283	80.346	352.805	355.912	349.842	328.321
19	Mamallapuram	12.462	80.156	352.805	355.912	349.842	328.321
20	Puducherry	12.040	79.872	351.102	355.912	349.842	328.321
21	-	11.672	79.759	351.102	355.912	349.842	328.321

Preprints (www.preprints.org) | NOT PEER-REVIEWED | Posted: 5 July 2022 doi:10.20944/preprints202207.0061.v1

22	Sirkazhi	11.196	79.857	351.102	349.842	349.842	328.321
23	-	10.308	79.880	341.777	349.842	349.842	328.321

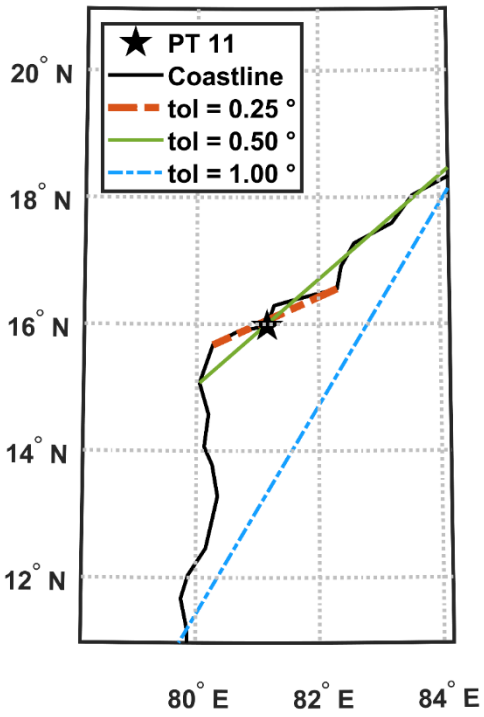

Figure 3. Linear approximations of the coastline at coastal point 11 for three different tolerance parameters of line simplification.

3.2. Estimation of Upwelling Indices

The wind and SST parameters were sampled at the coastal points to first compute ET and UI. The wind stresses were sampled at each of the 23 coastal points using a Cressman window with a radius of influence of 75 km [23], and ET was obtained from it following [20] as:

$$\tau_a = -\frac{abs(lat)}{lat}\left(\tau_x \cos\left(\theta - \frac{\pi}{2}\right) + \tau_y \sin\left(\theta - \frac{\pi}{2}\right)\right) \quad (1)$$

$$\mathrm{ET} = \frac{\tau_a}{\rho f} \quad (2)$$

where, τ_x is the zonal component of wind stress, τ_y is the meridional component of windstress, θ is the coastal angle (angle subtended by the vector normal to the shoreline, pointing seaward, clockwise with reference to the east), ρ is the density of water, f is the Coriolis parameter, and ET being the Ekman Transport.

It was necessary to compute a non-dynamical UI for inter-comparison and for this purpose we relied on the traditional SST-based approach adopted by [24] in their analysis of coastal upwelling along the SW coast of India [20]. The coastal upwelling was characterized based on the latitudinal temperature gradient given by the SST difference between a point on the coast and another point 5° offshore, at the same latitude. Similar approaches with the offshore points at the mid-ocean and 3° separation were also followed by [8, 25 – 26] in their analyses of the same upwelling system. The choice of 5° separation of the offshore point by [24] was based on the fact that the cross-shore width of the upwelling zone in the study region was about 350 – 400 km. A selection of 5° hence placed the offshore

Preprints (www.preprints.org) | NOT PEER-REVIEWED | Posted: 5 July 2022 doi:10.20944/preprints202207.0061.v1

points sufficiently far from the cold upwelled waters. Similar approaches were also adopted by [27 – 28] for the Benguela current coastal upwelling system. The variability of oceanographic conditions at the onshore and offshore points resulting from factors not associated with coastal upwelling could introduce some errors in the estimates and hence represented a key limitation of this approach.

For application to the coastal upwelling system considered in the present analysis, we used a longitude offset of 3° considering the fact that the width of the western BoB coastal upwelling zone was about 40 km [5]. Hence, the selection of the offshore point at a separation of 3° off the coast was sufficient to separate the offshore points from the cold upwelled waters in the study region. The difference between SST sampled at the coastal point and the SST sampled 3° offshore was the non-dynamic SST-based proxy UI [20, 24 – 28], represented as:

$$UI_{SST} = SST_{coast} - SST_{offshore} \quad (3)$$

Each of the variables here were presented and compared either in terms of the decadal mean climatology (constructed over 2009 to 2018) of the unfiltered signal or in terms of a complete filtered time-series. For the filtering of each time series data, a zero phase-shift band-pass Butterworth filter [29] of order 3 was used with lower and upper thresholds of 0.90 cycles/year and 2.5 cycles/year, respectively, as most of the data showed strong peaks around 1 cycle/year and 2 cycles/year. The results are discussed in the subsequent sections.

3.3. Analysis of SSHA

EOF analysis is a particularly effective tool for analyzing strongly correlated fields (such as met-ocean observations) with the capability of reducing a data vector $\boldsymbol{x}$ (consisting of x_k; k=1,…, K) into a set of M PCs denoted by $\boldsymbol{u}$ (consisting of u_m; m=1,…,M) such that each element of $\boldsymbol{u}$ is a linear combination of the elements of the anomaly of $\boldsymbol{x}$ ($\boldsymbol{x'} = \boldsymbol{x} - \overline{\boldsymbol{x}}$). These PCs satisfy two conditions; first, each PC capture the largest amount of variance of the data ($\boldsymbol{x}$), (i.e. the first PC (u_1) explains the largest amount of variance, the second PC (u_2) explains the largest variance remaining after removing u_1, and so on), and second, they are uncorrelated with each other. The PCs are uniquely determined by the projection of the data anomaly vector ($\boldsymbol{x'}$) on the eigenvectors of the covariance matrix of $\boldsymbol{x}$ ($\boldsymbol{e_m}$; $m = 1,..,M$) [30].

$$u_m = \boldsymbol{e_m^T}\,\boldsymbol{x'} = \sum_{k=1}^{K} e_{k,m}\, x'_k \,; m = 1,..,M \quad (4)$$

For 2 dimensional geophysical data, EOF analysis allows us to identify dominant modes of variability in a field which are coherent over large spatio-temporal scales. An EOF analysis could be used to decompose a field varying in both space and time into a set of fixed spatial patterns that vary in strength coherently over time. These fixed spatial patterns are the EOFs or PCs, while the temporal variation of each PC is given by its respective time series [31 – 32]. In our analysis, the full unfiltered SSHA spatial data was first detrended and subsequently used to determine the significant coherent modes of variability using EOF analysis. It is pertinent to mention that EOF analysis, which effectively captures coherent variations, is particularly suited for studies involving planetary scale phenomenon and were extensively used to observe and analyze atmospheric and oceanic planetary scale activity [33 – 36]. [37] has used EOF analysis of SSHA to characterize equatorial Rossby waves.

4. Results

4.1. Spatio-temporal Variability of Coastal Upwelling System in the Western Bay of Bengal

The temporal variation of ET along the coast and off shore transport resulting from AWS ispresented in Figure 4 for two different values of the tolerance parameter used to

Preprints (www.preprints.org) | NOT PEER-REVIEWED | Posted: 5 July 2022 doi:10.20944/preprints202207.0061.v1

compute the coastal angles. Figure 4(a) corresponds to a tolerance of 0.25° while B corresponds to a value of 1.0°. While a greater alongshore variation of ET was observed in the first case, both figures illustrate the ET to turn positive from April to May and persist up to September along the major part of the Indian east coast. Strongest ET was observed between points 6 – 8 (17.276 °N – 16.558 °N, i.e. around Kakinada, from the mouth of the Tandava river to the Lanka Island in the northern Godavari Delta in Andhra Pradesh), often extending further northward to point 1 (Palasa-Kasibugga). For a lower value of the tolerance parameter (Figure 4a), the ET along a southern stretch of the coast (point 13: Chinnaganjam (15.672 °N) to 17 (13.782 °N close to Sriharikota off Lake Pulicat) showed a more rapid increase in April, often reaching its maximum value by May (pre-monsoon) and declining through the SW monsoon months. The ET computed from the low tolerance parameter coastal angles agreed more closely with the temporal variability of UI_{SST} as in Figure 5. It was hence observed (by comparing Figure 4a and 4b), that an oversimplified coastline could lead to significant differences in the observed ET variability. We relied upon ET corresponding to the lowest tolerance parameter value of 0.25° for the analysis as this matched the grid spacing of the windstress data.

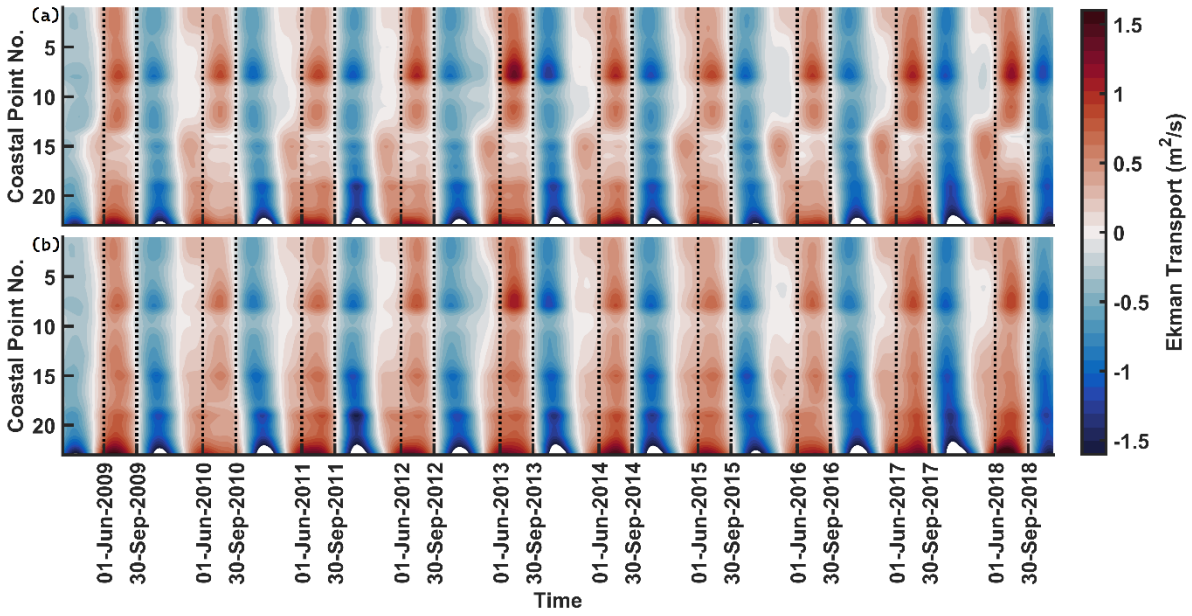

Figure 4. Temporal variation of ET along the coastline for coastal angles computed with tolerance parameter values of (a) 0.25° and (b) 1.0°.

The temporal variation of the UI_{SST} along the coast is illustrated in Figure 5. In this analysis, a negative value of the UI indicated the presence of relatively colder SST near the coast; a signature of coastal upwelling. Strong (negative) UI values were observed along the southern part of the coast between points 14 (15.074 °N) and 22 (11.196 °N) (north of Kavali to east of Sirkazhi, Tamil Nadu), between points 7 (16.909 °N) and 8 (16.558 °N), i.e. around Kakinada), and to the north of point 3 (i.e. 18.309 °N between Kalingapatnam and off Kashinagara). The UI value peaked between May and June months along the points 14 – 19 (16.558 °N – 12.462 °N i.e. to the south of Mamallapuram), and points 1 – 3 (between Kalingapatnam and off Kashinagara), while the peaks appeared in July and August along points 20 – 22 (12.040 °N – 11.196 °N, i.e. between the cities of Puducherry or Pondicherry and Sirkazhi), and points 7 and 8 (near Kakinada). Upwelling signals (negative UI) were not observed between points 9 (southern Godavari Delta) and 13 (Chinnaganjam) with moderate downwelling signals (positive UI) persisting at point 12.

Preprints (www.preprints.org) | NOT PEER-REVIEWED | Posted: 5 July 2022 doi:10.20944/preprints202207.0061.v1

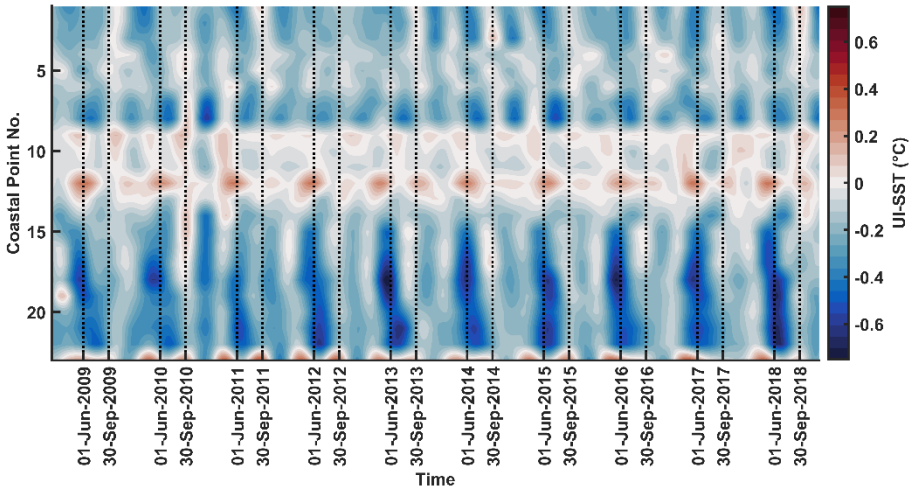

Figure 5. Temporal variation of SST-based UI (UI_{SST}) along the eastern coastline of India.

A decadal climatology (averaged over the years 2009 to 2018) of filtered ET, UI_{SST} and SSHA in the study region was generated (Figure 6). In the figure, the contours of UI_{SST} and SSHA were overlaid on the ET sampled at each coastal point. Coincident positive ET and negative UI (consistent with coastal upwelling) were observed at several discontinuous stretches along the coast (points 1-3, i.e. between Kalingapatnam and Palasa-Kasibugga, points 7-8 between Kakinada and the Lanka Island, and points 14-22 between Kavali and Sirkazhi). However, the negative SSHA typically associated with coastal upwelling events were not seen along most parts of the coast. The southern stretch of the coast (points 19 (Mamallapuram) – 22 (Sirkazhi)) showed coincident positive ET, negative UI and negative SSHA. Additionally, the strongest and most continuous UI_{SST} signatures were observed in the southern part of the coast (south of point 14 (Kavali)) during pre-monsoon (May) and earlier half of SW monsoon (June - July), although the strongest offshore transport (ET) was observed around point 6 – 8 (around Kakinada, AP). This indicated a possible partial suppression of coastal upwelling in the northern part of the coast (in comparison to the south coast) as the strong SST signatures of upwelling were only apparent in July – August (during the period of maximum ET).

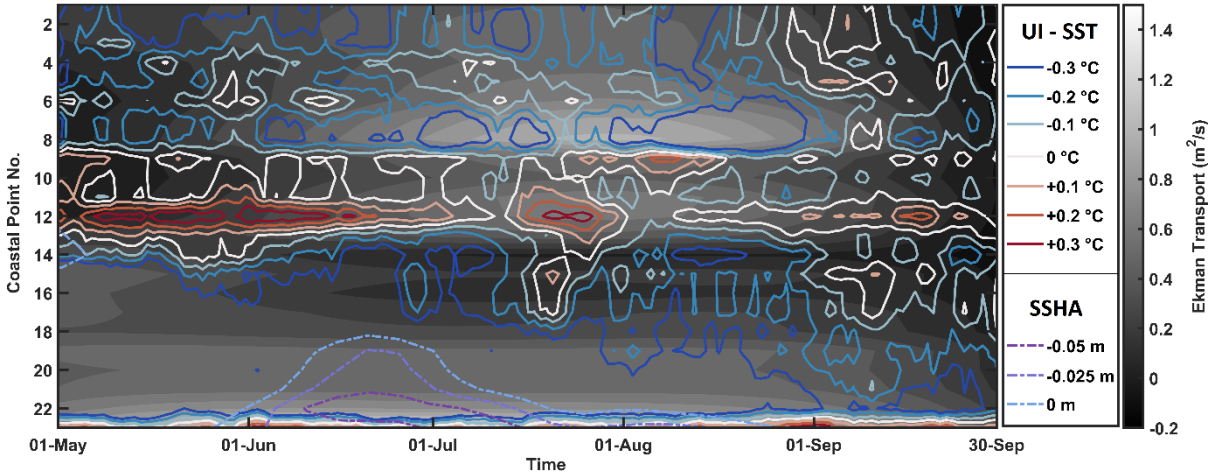

Figure 6. Climatology of ET (shaded in gray), with overlaid contours of SST based Upwelling Index (UI_{SST}: solid lines), and SSHA (dashed lines).

Preprints (www.preprints.org) | NOT PEER-REVIEWED | Posted: 5 July 2022 doi:10.20944/preprints202207.0061.v1

The sea levels and circulation in the BoB are determined by both local and remote wind forcing during the SW monsoon [38]. A prominent remote forcing mechanism in this region consisted of two upwelling and two downwelling Kelvin waves which propagate eastward along the coastal waveguide of the BoB [39]. These waves are generated near the equator due to the reflection of eastward propagating equatorial Kelvin waves. In addition, coastal Kelvin waves could also be triggered by coastal upwelling along the margins of the Bay [40]. Therefore, it was necessary to further analyse the coastal upwelling related SSHA variations during the monsoon time period to understand the mechanism better. We therefore analysed the coastally trapped Kelvin wave activity along the western margin of the BoB based on the decadal climatology of SSHA.

4.2. Coastally trapped Kelvin wave activity

SSHA variations contain distinct signatures of propagating planetary scale waves including the subsurface variations associated with them [41]. Following [42], we first located the activity of upwelling and downwelling coastally trapped Kelvin waves in the region using the long-term mean SSHA variability. Upwelling Kelvin waves are associated with negative coastal SSHA, while downwelling Kelvin waves are associated with positive coastal SSHA signatures. The 10-year mean (climatology) SSHA from 2009 to 2018 are presented in Figures 7 and 8 for every other 5 day period (the temporal resolution of the data being 5 days). It was observed that the coastal BoB experienced two sets of upwelling and downwelling Kelvin waves that propagated counter clock-wise starting from the coast of Sumatra in the east up to the coast of Tamil Nadu and Sri Lanka. The SW monsoon period (months of June, July, August & September, JJAS) considered here covered the period of activity of two of the four Kelvin waves: the first downwelling Kelvin wave and the second upwelling Kelvin wave [42].

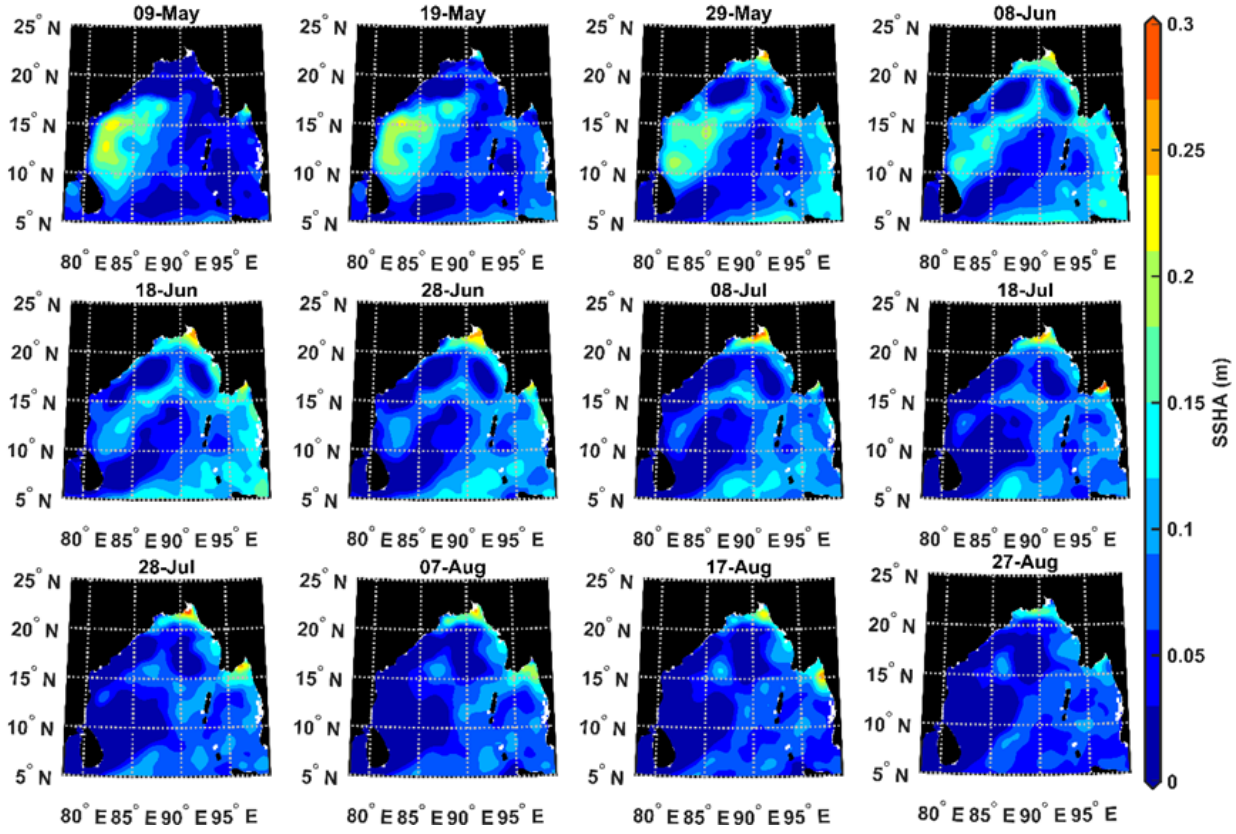

Figure 7. Decadal Climatology (2009 to 2018) of positive SSHA corresponding to the first downwelling Kelvin wave activity.

Preprints (www.preprints.org) | NOT PEER-REVIEWED | Posted: 5 July 2022 doi:10.20944/preprints202207.0061.v1

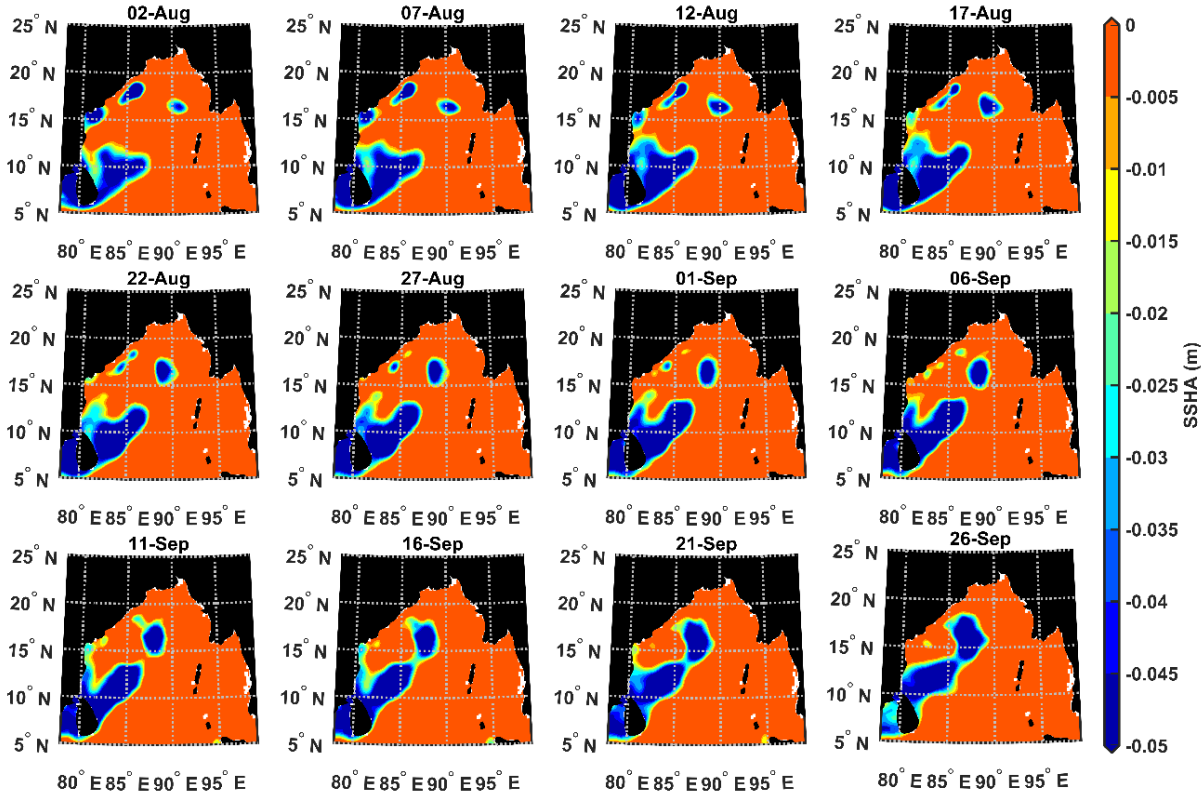

Figure 8. Decadal Climatology (2009 to 2018) of negative SSHA corresponding to the second upwelling Kelvin wave period.

Positive SSHAs were observed prominently from mid to late May at the head Bay region along the coast of West Bengal and Bangladesh and along the eastern BoB. These anomalies could be observed in the region throughout the season, persisting up to the middle of August. During mid to late June, positive SSHAs were also observed along the north-western margin of BoB down to 18 °N. Negative SSHA signals first appeared along the western boundary of the BoB, along the coast of India, near 15 °N in early August. The anomalies then propagated southward, first along the coast of India and then around Sri Lanka, into the Arabian Sea. Since, it was difficult to isolate the signal corresponding to coastally trapped Kelvin wave activity from the SSHA fields directly, an EOF analysis of SSHA data was carried out to observe these variations distinctly. In the following sections, we attempt to identify PCs of SSHA associated with these Kelvin wave signatures.

4.3. EOF Analysis of SSHA

It was observed that the first 6 PCs (or EOFs) could cumulatively explain 59.23% of the variance in SSHA. Among these, the first three modes alone could cumulatively explain 47.32 % of the variance (presented in Figure 9) revealing coastally bound SSHA signatures with low alongshore variability. The first three PCs also illustrated a greater magnitude of variation of the PC time series compared to the remaining three. We, therefore, focused on the first three PCs for further detailed analysis. The first PC consisted of strong positive SSHA (0.2 – 0.5 m) at the head of the Bay and along its eastern margins; this was similar to the signature associated with the first downwelling Kelvin wave during June – July (Figure 7). The third PC was associated with a comparatively weaker positive SSHA (about 0.1 m) along the western margin of the BoB, with relatively stronger signals to the south of 16.250 °N. This was similar in terms of the spatial distribution to the negative

Preprints (www.preprints.org) | NOT PEER-REVIEWED | Posted: 5 July 2022 doi:10.20944/preprints202207.0061.v1

SSHA associated with the second upwelling Kelvin wave, implying that a negative PC time series resulted in SSHA patterns similar to the second upwelling Kelvin wave signatures (Figure 8). The eastward spread of SSHA around 10 °N, and the westward spread around Sri Lanka towards the Arabian Sea are noticeable in both Figures 8 and 9C. The second PC was similar to the third PC along the coast of India, however, coastal SSHA signatures were weaker (around 0.05 m) and limited within a smaller cross-shore distance from the coast.

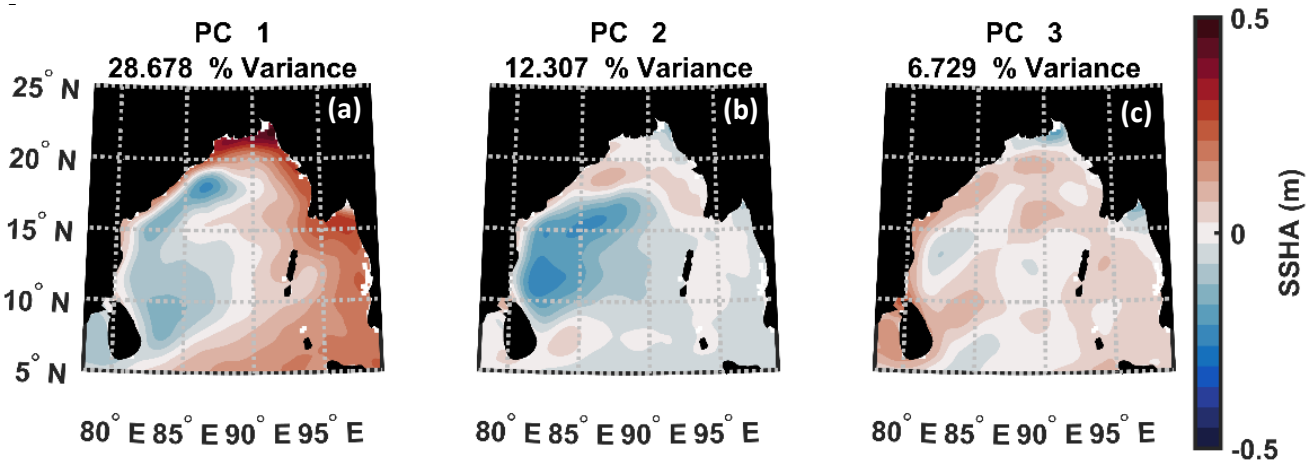

Figure 9. First 3 Principal Components of SSHA in the study region: (a) PC1, (b) PC2, and (c) PC3.

The decadal mean variation of the first three PCs is illustrated in Figure 10(a) while the filtered time series for each individual year is presented in Figure 10(b). The climatology of these three PC time series varied within the range of ±0.55, although the magnitude of the coastal anomaly associated with each PC was different. The PCs were scaled to vary between ±1 following [43], by dividing each PC by its maximum value and multiplying the EOF maps by the same.

As all three PCs obtained in the preceding analysis consisted of positive coastal SSHA. A negative (positive) value of the PC time series was likely to be associated with upwelling (downwelling) signatures. PC 1 showed a strong negative signature (< 0.5) around March which is the period when the first upwelling Kelvin wave was active. However, the signal remained weakly positive during the subsequent part of the year, varying in the range of 0.12 to 0.34. The second PC showed a clear annual cycle with a trough in late May and a peak in late November. The third PC revealed two sets of peaks and troughs; a smaller trough (-0.12) appearing in late March (shortly after the trough of the first PC), followed by a smaller peak (0.20) in the middle of May. The larger trough (- 0.53) then appeared in early August followed by the larger peak (0.56) towards the end of December. Thus, the smaller peak of the third PC and the largest peak of the first PC occurred in May and June, respectively, i.e. during the period of activity of the first downwelling Kelvin wave. The largest trough of the third PC however occurred in August which was also the period of activity of the second upwelling Kelvin wave.

Preprints (www.preprints.org) | NOT PEER-REVIEWED | Posted: 5 July 2022 doi:10.20944/preprints202207.0061.v1

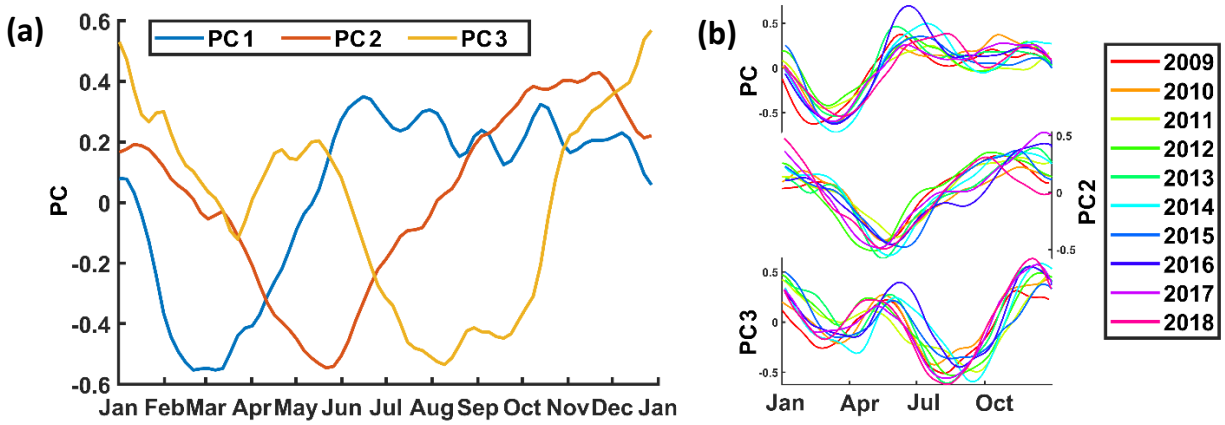

Figure 10. (a) Decadal mean variability of first three PCs of SSHA, (b) Temporal variation of first 3 PCs.

It was observed that the first PC initially peaked in the earlier part of the SW monsoon season (June – July), and then remained weakly positive during the rest of the season, i.e. August and September (Figure 10). The decadal mean of the first PC peaked in the middle of June, weakening partially in July (varying between 0.23 - 0.30), and weakening further in August (varying between 0.15 – 0.23), reaching its lowest monsoon value of 0.12 in mid-September. In the years 2011, 2012 and 2014, the first PC turned weakly negative (> -0.1) towards the end of September or in early October. In 2018, the positive value extended late into monsoon, with positive values as high as 0.38 persisting upto August, and 0.13 up to September. The trough of the third PC, with a magnitude of -0.4 to -0.6 typically occurred in August (September in 2011 and 2014). The most negative magnitudes of the third PC were observed during the years 2013 and 2018, while the first PC remained positive throughout the SW monsoon in both these years. The second PC switched from negative to positive over the course of SW monsoon and was relatively weaker (< 0.3) during peak monsoon activity (strong ET and UI) during July – August. This indicated that the second upwelling Kelvin wave signatures along the western boundary of the BoB were not closely related with upwelling signatures along the eastern boundary and head of the Bay. Thus, it was seen that the first and third PCs closely matched the temporal span of the first downwelling and second upwelling Kelvin wave activity, respectively. Thus, the PCs of SSHA exhibited a close spatio-temporal association with the coastal Kelvin waves signatures.

5. Discussions

In our analysis of the BoB coastal upwelling system along the coast of India, the temporal variation of ET and UI_{SST} were first analyzed. Having established the close association between the PCs of SSHA and coastal Kelvin waves, analysis of the spatio-temporal variability of BoB coastal upwelling also presented interesting results as disussed here. While comparing the climatological distribution of ET and UI, collocated instances of high positive ET and negative UI (both indicative of coastal upwelling) were observed at different stretches of the coast during the SW monsoon season (Figure 5), with two main peculiarities evident in the analysis (Figure 6). First, the negative SSHA, which is typically associated with coastal upwelling systems was found only in the southern-most part of the Indian coast. Second, the northern section of the coast illustrated a poorer UI_{SST} response relative to the southern section in spite of comparable ET. The absence of negative SSHA in the northern section of the coast could be associated with near-shore eddies generated from the east India coastal current or excess river discharge [44]. The SSHA variations during May and the SW monsoon months (JJAS) showed the existence of both the first downwelling Kelvin wave (evident in Figure 7) and the second upwelling Kelvin wave (noticeable in Figure 8). An EOF analysis of SSHA revealed two dominant PCs that

Preprints (www.preprints.org) | NOT PEER-REVIEWED | Posted: 5 July 2022 doi:10.20944/preprints202207.0061.v1

were closely associated with the coastal Kelvin wave activity observed from the long-term mean SSHA, spatially and temporally.

It is well known that the westerly (easterly) zonal winds at the equator generate eastward propagating downwelling (upwelling) Kelvin waves in the region that are obstructed by the Sumatra islands, which then propagate along the coastal waveguide of the BoB [45 – 47]. Therefore, the cross-correlation between the first PC (consisting of strong SSHA near the head of the Bay and along its eastern margins) and equatorial zonal wind forcing (mean zonal windstress forcing between 0 ° to 5 °N and 40 °E to 90 °E) was analysed to further ascertain the association of this PC and coastally trapped Kelvin wave activity (Figure 11). A maximum correlation of 0.734 was observed with the first PC lagging behind the equatorial wind forcing by 20 days while the other two PCs illustrated a much lower correlation. This revealed a close agreement between the spatio-temporal extent of the first PC and the first downwelling Kelvin wave. Thus, in addition to being spatio-temporally coincident with the first downwelling Kelvin wave, this PC also showed a close association with equatorial zonal winds (Figure 11) which are known to drive the equatorial Kelvin waves, which in turn drive the coastally trapped Kelvin waves [42].

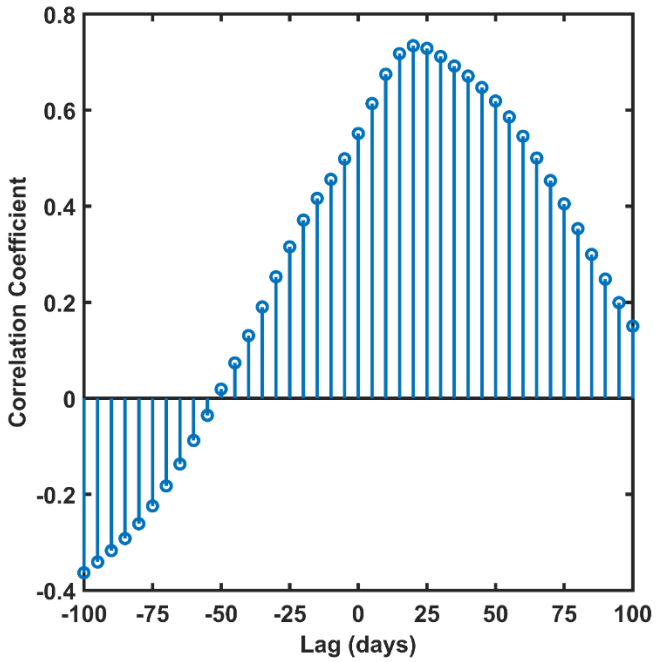

Figure 11. Cross-correlation of first PC of SSHA and equatorial zonal wind forcing.

While the third PC closely matched the spatio-temporal extent of the second upwelling Kelvin wave, it should be noted that this Kelvin wave was largely restricted to the south-eastern margin of the BoB. Further, the local AWS forced ET (coastal upwelling) played a dominant role in modulating this Kelvin wave [42]. The cross-correlation analysis between the third PC and the local AWS driven ET at each of the 23 coastal points was helpful to ascertain the actual driving mechanism of the coastal upwelling in the study region (Figure 12). The strongest negative correlation (< - 0.75) was observed at points 6 (mouth of Thandava river) – 12 (south of Machilipatnam), i.e. between 17.267 °N and 15.889 °N at a lag of 1 – 7 days (PC 3 lagged behind ET). Points 6 – 8 (northern Godavari delta, around Kakinada) were also prominently noticeable in the climatology of ET, UI_{SST} and SSHA presented in Figure 6 as it represented the strongest ET and a moderately high UI_{SST} was strongly correlated with the ET. This indicated that the SSHA signatures associated with the second upwelling Kelvin wave [42] as in Figure 8, were largely driven by the local AWS forced ET between 15.889 – 17.276 °N (between the mouth of Thandava

Preprints (www.preprints.org) | NOT PEER-REVIEWED | Posted: 5 July 2022 doi:10.20944/preprints202207.0061.v1

river to the south of Machilipatnam). [42] also previously noted that local AWS could influence and trigger these Kelvin waves. Our analysis strongly indicated the existence of coastal SSHA signatures associated with the second upwelling Kelvin wave, which were largely driven by ET forced by local AWS along the south-eastern coast of India. Further, these had a negligible effect of equatorial remote forcing.

While the coastal SSHA remained positive through most of SW monsoon along the coast north of point 18 (near Ennore port), a dominant coherent empirical mode of variation consisting of negative coastal SSHA were excited in response to local AWS driven ET (particularly between points 6 – 12 (between the mouth of Thandava river to the south of Machilipatnam). Although, the strongest ET response existed in the north, this part of the coast remained under the influence of the first downwelling Kelvin wave through most of the SW monsoon season (up to August). Thus, strong upwelling signals (UI_{SST}) were observed only intermittently between points 6 and 8 (around Kakinada) (maximum ET), over a very short span of time (July – August) during the maximum local AWS forced ET.

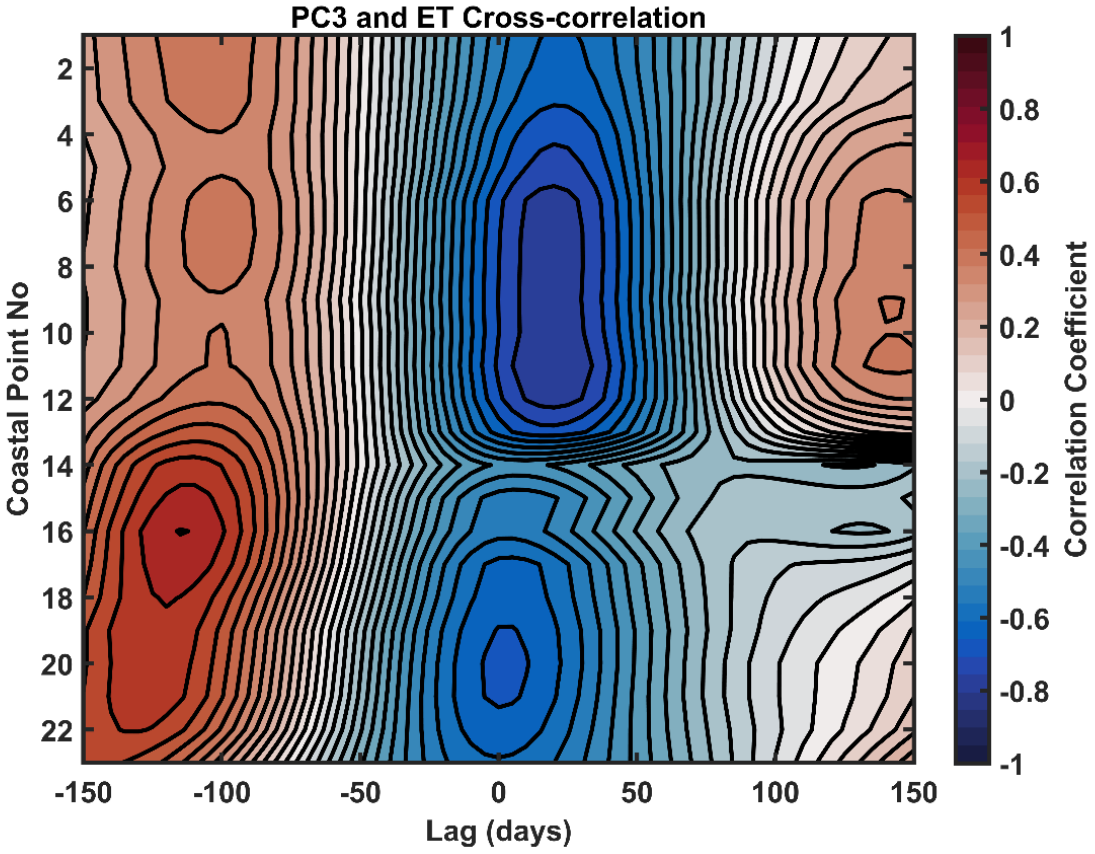

Figure 12. Cross-correlation of third PC and local ET along the east coast of India.

6. Conclusions

UI_{SST}, and ET signatures during most of SW monsoon (JJAS) were indicative of coastal upwelling at different stretches along the coast. The strongest coastal upwelling was observed to occur in the southern part of the coast (south of 15.074 °N, i.e. Kavali) during May to July. This receded farther south and was restricted south of 13.283 °N (Ennore port) in August, but continued to still recede further south through September. Strong ET was observed only along the northern part of the Indian east coast (north of 16.558 °N near Lanka Island, northern Godavari Delta), with the highest values within 17.276 – 16.558 °N (around Kakinada) between July and August months.

Monsoon coastal circulation in the BoB was closely linked to the remotely forced coastally trapped Kelvin wave activity which propagated anti-clockwise along the margin of the Bay in two cycles each consisting of one upwelling and one downwelling Kelvin waves. EOF analysis of the SSHA data revealed two distinct spatial modes of variability or PCs associated with the Kelvin wave activity. An analysis of the PC time series of the first and third PC reveals that during late May and the earlier part of SW monsoon (June–July); the remotely forced first downwelling Kelvin wave excited positive coastal SSHA around the northern parts of the eastern and western margins, and the head of the BoB. Thus, it was evident that the remotely forced coastally trapped Kelvin waves suppressed the intensity of coastal upwelling despite the presence of moderately strong ET in the northern part of the Indian east coast adjoining the BoB (relative to the south). In July – August, strong locally driven coastal upwelling was observed along large parts of the northern section of the coast, as the effect of remotely forced Kelvin waves weakened partly. This was evident from the analysis of climatology (Figure 6), PC of SSHA (Figures 9 & 10), and the correlation of the third PC with local AWS (Figure 12). However, by September, the ET also reduced and strong UI_{SST} signals were therefore not observed. The BoB coastal upwelling system is considered a classic local AWS driven coastal upwelling system similar to the EBUS. While this was found to be true, remote forcing of equatorial zonal windstress appeared to play a significant role in modulating the intensity of upwelling along the coast as evident in the present analysis. In addition, our analysis also established the fact that coherent spatial modes consisting of negative coastal SSHA were indeed excited during the SW monsoon period along with upwelling-favouring ET and SST conditions, although the SSHA remained positive.

Several other aspects of this system may be addressed in future studies; for e.g., the high frequency variations associated with each of these upwelling indicators could be analyzed. The second PC could also be analyzed in terms of the alongshore currents. It is possible that the alongshore currents play a role in the separation of the coastal jet from the shore. Additionally, the westward propagation of Kelvin waves around Sri Lanka into the Arabian Sea may be investigated following techniques similar to ours.

Acknowledgements: The computation and data analysis has been carried out on Matlab 2021a with the Climate Data Toolbox [48] and the Douglas-Peucker line simplification algorithm implemented in Matlab by Schwanghart [49]. The authors thank IIT Bhubaneswar for facilitating the research work. SR was partially supported through a fellowship from SAC/ISRO and gratefully acknowledges the same.

Funding: No external funding was received for carrying out the work.

Author Contributions: SR and DS have conceptualized the work; SR has carried out the analysis. SR and DS have written the manuscript with inputs from MMA and MAB. All the authors have contributed to revise the manuscript.

Data Availability Statement: All the data sets used in the study are available free of cost through their respective websites.

Conflicts of Interest: The authors declare no conflict of interest.

Highlights:

- A parametric method for estimation of coastal angles was developed; the ET calculated using coastal angles computed with the lowest value of the tolerance parameter (0.25°) were found to be agreeable with the observed SST-based UI (UI_{SST}).
- High AWS and coincident strong negative UI_{SST} (indicative of coastal upwelling) were observed from the pre-monsoon period in the south and from monsoon along the northern part of the east coast of India.

- The northern part of the coast illustrated relatively weaker and temporally restricted UI$_{SST}$ response compared to the south.
- The equatorial windstress forced first downwelling Kelvin wave suppressed coastal upwelling, especially in the northern part of the coast during June and July.
- The second upwelling Kelvin wave, largely driven by AWS along the northern part of the east coast of India, was associated with negative coastal SSHA in the late monsoon coincident with other coastal upwelling signatures.

References

1. Bakun, A.; Black, B. A.; Bograd, S. J.; García-Reyes, M.; Miller, A. J.; Rykaczewski, R. R.; Sydeman, W. J. Anticipated Effects of Climate Change on Coastal Upwelling Ecosystems. Curr Clim Change Rep. 2015, 1 (2), 85–93. https://doi.org/ 10.1007/ s40641-015-0008-4.
2. Botsford, L. W.; Lawrence, C. A.; Dever, E. P.; Hastings, A.; Largier, J. Effects of Variable Winds on Biological Productivity on Continental Shelves in Coastal Upwelling Systems. Deep Sea Res. Part II 2006, 53 (25–26), 3116–3140.
3. Hu, J.; Wang, X. H. Progress on Upwelling Studies in the China Seas. Rev. Geophys. 2016, 54 (3), 653–673.
4. Kämpf, J.; Chapman, P. Upwelling Systems of the World; Springer: Switzerland, 2016.
5. Shetye, S. R.; Shenoi, S. S. C.; Gouveia, A. D.; Michael, G. S.; Sundar, D.; Nampoothiri, G. Wind-Driven Coastal Upwelling along the Western Boundary of the Bay of Bengal during the Southwest Monsoon. Cont. Shelf Res. 1991, 11 (11), 1397–1408.
6. Sarma, Y. V. B.; Rao, E. R.; Saji, P. K.; Sarma, V. Hydrography and Circulation of the Bay of Bengal during Withdrawal Phase of the Southwest Monsoon. Oceanolog. Acta 1999, 22 (5), 453–471.
7. Santosh, K. M.; Reddy, H. R. V.; Padiyar, A. Hydrography of the Bay of Bengal during South West Monsoon and Its Significance on Oil Sardine Fishery. Bangladesh J. Fisheries Res. 2002, 6 (1), 69–74.
8. Muni Krishna, K. View on Bay of Bengal Upwelling Area on the Basis of 19-Years of Satellite Sea Surface Temperature. Int. J. Digital Earth 2008, 1 (3), 304–314.
9. Patel, S.; Vithalpura, M.; Mallick, S. K.; Ratheesh, S. Temporal and Spatial Variations of Monsoonal Upwelling along the South West and East Coasts of India. Marine Geodesy 2020, 43 (4), 414–432.
10. Bentamy, A.; Piolle, J. F.; Prevost, C. PRODUCT USER MANUAL For Wind Product WIND_GLO_WIND_L4_REP_OBSERVATIONS_012_006; CMEMS-WIND-PUM-012-006; Copernicus Marine Service, 2021.
11. Bentamy, A. QUALITY INFORMATION DOCUMENT For Wind Product WIND_GLO_WIND_L4_REP_OBSERVATIONS_012_006; CMEMS-WIND-QUID-012-006; Copernicus Marine Service, 2021.
12. Worsfold, M.; Good, S.; Martin, M.; McLaren, A.; Roberts-Jones, J.; Fielder, E. QUALITY INFORMATION DOCUMENT Global Ocean OSTIA Sea Surface Temperature Reprocessing SST-GLO-SST-L4-REP-OBSERVATIONS-010-011; CMEMS-WIND-PUM-012-006; Copernicus Marine Service, 2021.
13. Worsfold, M.; Good, S.; Martin, M.; McLaren, A.; Roberts-Jones, J.; Fielder, E. PRODUCT USER MANUAL Global Ocean OSTIA Sea Surface Temperature Reprocessing SST-GLO-SST-L4-REP-OBSERVATIONS-010-011; CMEMS-WIND-PUM-012-006; Copernicus Marine Service, 2021.
14. Beckley, B. D.; Zelensky, N. P.; Holmes, S. A.; Lemoine, F. G.; Ray, R. D.; Mitchum, G. T.; Desai, S. D.; Brown, S. T. Assessment of the Jason-2 Extension to the TOPEX/Poseidon, Jason-1 Sea-Surface Height Time Series for Global Mean Sea Level Monitoring. Marine Geodesy 2010, 33 (sup1), 447–471. https://doi.org/10.1080/ 01490419. 2010.491029.
15. Zlotnicki, V.; Qu, Z.; Willis, J.; Ray, R.; Hausman, J. JPL MEASURES Gridded Sea Surface Height Anomalies Version 1812; https://doi.org/10.5067/SLREF-CDRV2; PO.DAAC, CA, USA, 2019.
16. Wessel, P.; Smith, W. H. A Global, Self-consistent, Hierarchical, High-resolution Shoreline Database. J. Geophys. Res.: Solid Earth 1996, 101 (B4), 8741–8743.
17. Bakun, A. Coastal Upwelling Indices, West Coast of North America, 1946-71; 671; US Dept. Commerce NOAA Tech. Rep. NMFS-SSRF, 1973; pp 1–103.
18. Benazzouz, A.; Mordane, S.; Orbi, A.; Chagdali, M.; Hilmi, K.; Atillah, A.; Lluís Pelegrí, J.; Hervé, D. An Improved Coastal Upwelling Index from Sea Surface Temperature Using Satellite-Based Approach – The Case of the Canary Current Upwelling System. Cont. Shelf Res. 2014, 81, 38–54. https://doi.org/10.1016/j.csr.2014.03.012.
19. Shetye, S. R. Seasonal Variability of the Temperature Field off the South-West Coast of India. Proceedings of the Indian Academy of Sciences. Earth Planet. Sci. 1984, 93 (4), 399–411.
20. Jayaram, C.; Kumar, P. D. Spatio-Temporal Variability of Upwelling along the Southwest Coast of India Based on Satellite Observations. Cont. shelf res. 2018, 156, 33–42.
21. Roberts, M. J.; Nieuwenhuys, C. Observations and Mechanisms of Upwelling in the Northern KwaZulu-Natal Bight, South Africa. Afr. J. Mar. Sci. 2016, 38 (sup1), S43–S63.
22. Douglas, D. H.; Peucker, T. K. Algorithms for the Reduction of the Number of Points Required to Represent a Digitized Line or Its Caricature. Cartographica: Int. J. Geograp. Info. Geovisual. 1973, 10 (2), 112–122.
23. Cressman, G. P. An Operational Objective Analysis System. Mon. Weather Rev. 1959, 87 (10), 367–374.

24. Jayaram, C.; Chacko, N.; Joseph, K. A.; Balchand, A. N. Interannual Variability of Upwelling Indices in the Southeastern Arabian Sea: A Satellite Based Study. Ocean Sci. J. 2010, 45 (1), 27–40.
25. Naidu, P. D.; Kumar, M. R.; Babu, V. R. Time and Space Variations of Monsoonal Upwelling along the West and East Coasts of India. Cont. Shelf Res. 1999, 19 (4), 559–572.
26. Smitha, B. R.; Sanjeevan, V. N.; Vimalkumar, K. G.; Revichandran, C. On the Upwelling off the Southern Tip and along the West Coast of India. J. Coastal Res. 2008, No. 24 (10024), 95–102.
27. Santos, F.; Gomez-Gesteira, M.; Decastro, M.; Alvarez, I. Differences in Coastal and Oceanic SST Trends Due to the Strengthening of Coastal Upwelling along the Benguela Current System. Cont. Shelf Res. 2012, 34, 79–86.
28. Marcello, J.; Hernandez-Guerra, A.; Eugenio, F.; Fonte, A. Seasonal and Temporal Study of the Northwest African Upwelling System. Int. J. Remote Sens. 2011, 32 (7), 1843–1859.
29. Roberts, J.; Roberts, T. D. Use of the Butterworth Low-pass Filter for Oceanographic Data. J. Geophys. Res.: Oceans 1978, 83 (C11), 5510–5514.
30. Wilks, D.S. Chapter 12 - Principal Component (EOF) Analysis. In International Geophysics; Wilks, D.S., Ed.; Statistical Methods in the Atmospheric Sciences; Academic Press, 2011; Vol. 100, pp. 519–562.
31. Björnsson, H.; Venegas, S.A. A Manual for EOF and SVD Analyses of Climatic Data; Department of Atmospheric and Oceanic Sciences and Center for Climate and Global Change Research, McGill University, 1997; pp. 112–134.
32. Preisendorfer, R. Principal Component Analysis in Meteorology and Oceanography. Elsevier Sci. Publ. 1988, 17, 425.
33. Pratt, R. W.; Wallace, J. M. Zonal Propagation Characteristics of Large–Scale Fluctuations in the Mid–Latitude Troposphere. J. Atmos. Sci. 1976, 33 (7), 1184–1194. https://doi.org/10.1175/1520-0469(1976)033<1184:ZPCOLF>2.0.CO;2.
34. Trenberth, K. F. Atmospheric Quasi-Biennial Oscillations. Mon. Weather Rev. 1980, 108 (9), 1370–1377. https://doi.org/10.1175/1520-0493(1980) 108<1370:AQBO> 2.0. CO;2.
35. Feng, M.; Meyers, G.; Wijffels, S. Interannual Upper Ocean Variability in the Tropical Indian Ocean. Geophys. Res. Lett. 2001, 28 (21), 4151–4154. https://doi.org/ 10. 1029 /2001GL013475.
36. Hannachi, A. Tropospheric Planetary Wave Dynamics and Mixture Modeling: Two Preferred Regimes and a Regime Shift. J. of the Atmos. Sci. 2007, 64 (10), 3521–3541. https://doi.org/10.1175/JAS4045.1.
37. Rydbeck, A. V.; Jensen, T. G.; Flatau, M. K. Reciprocity in the Indian Ocean: Intraseasonal Oscillation and Ocean Planetary Waves. J. Geophys. Res.: Oceans 2021, 126 (9), e2021JC017546. https://doi.org/10.1029/2021JC017546.
38. Shankar, D.; Vinayachandran, P.N.; Unnikrishnan, A.S. The Monsoon Currents in the North Indian Ocean. Progress in oceanography 2002, 52, 63–120.
39. Yu, L.; O'Brien, J. J.; Yang, J. On the Remote Forcing of the Circulation in the Bay of Bengal. J. Geophys. Res.: Oceans 1991, 96 (C11), 20449–20454.
40. McCreary Jr, J. P.; Kundu, P. K.; Molinari, R. L. A Numerical Investigation of Dynamics, Thermodynamics and Mixed-Layer Processes in the Indian Ocean. Prog. Oceanogr. 1993, 31 (3), 181–244.
41. Fu, L.-L. Ocean Circulation and Variability from Satellite Altimetry. In International Geophysics; Elsevier, 2001; Vol. 77, pp. 141–XXVIII ISBN 0074-6142.
42. Rao, R. R.; Kumar, M. G.; Ravichandran, M.; Rao, A. R.; Gopalakrishna, V. V.; Thadathil, P. Interannual Variability of Kelvin Wave Propagation in the Wave Guides of the Equatorial Indian Ocean, the Coastal Bay of Bengal and the Southeastern Arabian Sea during 1993–2006. Deep Sea Res. Part I 2010, 57 (1), 1–13.
43. Messié, M.; Chavez, F. Global Modes of Sea Surface Temperature Variability in Relation to Regional Climate Indices. J. Clim. 2011, 24 (16), 4314–4331.
44. Dandapat, S.; Gnanaseelan, C.; Parekh, A. Impact of Excess and Deficit River Runoff on Bay of Bengal Upper Ocean Characteristics Using an Ocean General Circulation Model. Deep Sea Res. Part II 2020, 172, 104714.
45. McPhaden, M. J. Variability in the Central Equatorial Indian Ocean. I. Ocean Dynamics. J. Mar. Res. 1982, 40 (1), 157–176.
46. Jensen, T. G. Equatorial Variability and Resonance in a Wind-driven Indian Ocean Model. J. Geophys. Res.: Oceans 1993, 98 (C12), 22533–22552.
47. Miyama, T.; McCreary Jr, J. P.; Sengupta, D.; Senan, R. Dynamics of Biweekly Oscillations in the Equatorial Indian Ocean. J. Phys. Oceanogr. 2006, 36 (5), 827–846.
48. Greene, C. A.; Thirumalai, K.; Kearney, K. A.; Delgado, J. M.; Schwanghart, W.; Wolfenbarger, N. S.; Thyng, K. M.; Gwyther, D. E.; Gardner, A. S.; Blankenship, D. D. The Climate Data Toolbox for MATLAB. Geochem. Geophys. Geosyst. 2019, 20(7), 3774-3781, https://doi.org/10.1029/2019GC008392
49. Schwanghart, W. Line Simplification (https://www.mathworks.com/matlabcentral /fileexchange/21132-line-simplification), MATLAB Central File Exchange. 2021 (accessed 2021-09-28).